International Journal of Nanomedicine

Dovepress
open access to scientific and medical research

Open Access Full Text Article

ORIGINAL RESEARCH

Antioxidant Carbon Dots and Ursolic Acid Co-Encapsulated Liposomes Composite Hydrogel for Alleviating Adhesion Formation and Enhancing Tendon Healing in Tendon Injury

Cheng Peng[1,2], Shiqi Kang[1,2], Meijun Jiang[1,2], Mingxi Yang[1,2], Xu Gong[1,2]

[1]Department of Hand and Podiatric Surgery, Orthopedics Center, The First Hospital of Jilin University, Jilin University, Changchun, 130021, People's Republic of China; [2]Jilin Province Key Laboratory on Tissue Repair, Reconstruction and Regeneration, The First Hospital of Jilin University, Jilin University, Changchun, 130021, People's Republic of China

Correspondence: Xu Gong; Mingxi Yang, Email gongxu@jlu.edu.cn; yangmxchem@jlu.edu.cn

Background: The formation of adhesion after tendon injury represents a major obstacle to tendon repair, and currently there is no effective anti-adhesion method in clinical practice. Oxidative stress, inflammation, and fibrosis can occur in tendon injury and these factors can lead to tendon adhesion. Antioxidant carbon dots and ursolic acid (UA) both possess antioxidant and anti-inflammatory properties. In this experiment, we have for the first time created RCDs/UA@Lipo-HAMA using red fluorescent carbon dots and UA co-encapsulated liposomes composite hyaluronic acid methacryloyl hydrogel. We found that RCDs/UA@Lipo-HAMA could better attenuate adhesion formation and enhance tendon healing in tendon injury.

Materials and Methods: RCDs/UA@Lipo-HAMA were prepared and characterized. In vitro experiments on cellular oxidative stress and fibrosis were performed. Reactive oxygen species (ROS), and immunofluorescent staining of collagens type I (COL I), collagens type III (COL III), and α-smooth muscle actin (α-SMA) were used to evaluate anti-oxidative and anti-fibrotic abilities. In vivo models of Achilles tendon injury repair (ATI) and flexor digitorum profundus tendon injury repair (FDPI) were established. The major organs and blood biochemical indicators of rats were tested to determine the toxicity of RCDs/UA@Lipo-HAMA. Biomechanical testing, motor function analysis, immunofluorescence, and immunohistochemical staining were performed to assess the tendon adhesion and repair after tendon injury.

Results: In vitro, the RCDs/UA@Lipo group scavenged excessive ROS, stabilized the mitochondrial membrane potential (ΔΨm), and reduced the expression of COL I, COL III, and α-SMA. In vivo, assessment results showed that the RCDs/UA@Lipo-HAMA group improved collagen arrangement and biomechanical properties, reduced tendon adhesion, and promoted motor function after tendon injury. Additionally, the expression of nuclear factor erythroid 2-related factor 2 (Nrf2) and heme oxygenase 1 (HO-1) in the RCDs/UA@Lipo-HAMA group increased; the levels of cluster of differentiation 68 (CD68), inducible Nitric Oxide Synthase (iNOS), COL III, α-SMA, Vimentin, and matrix metallopeptidase 2 (MMP2) decreased.

Conclusion: In this study, the RCDs/UA@Lipo-HAMA alleviated tendon adhesion formation and enhanced tendon healing by attenuating oxidative stress, inflammation, and fibrosis. This study provided a novel therapeutic approach for the clinical treatment of tendon injury.

Keywords: tendon adhesion, antioxidant, carbon dots, ursolic acid, liposomes, hydrogel

Introduction

Tendons are pivotal in facilitating joint motion by transmitting tensile loads, and tendon injuries often lead to a loss of joint mobility. The outcomes of tendon repairs remain suboptimal due to the formation of scar tissue at the repair site, known as adhesion formation. The tendon adhesion formation is an inevitable consequence of the tendon healing mechanisms.[1–3] Tendon healing occurs in three overlapping yet distinct phases: the inflammatory phase, the proliferative

Received: 17 April 2024
Accepted: 10 August 2024
Published: 27 August 2024

phase, and the remodeling phase.[4] The presence of an inflammatory response in tendon healing, coupled with the limited regenerative capacity of tenocytes, means that tendon repair typically depends on the deposition of connective tissue, which ultimately leads to scar tissue adhesion formation.[5]

In the clinical setting, the strategy to ameliorate tendon adhesion is the early active or passive mobilization protocols. Unfortunately, it is estimated that at least one-third of patients with tendon injuries end up in varying degrees of adhesion formation.[6,7] Additionally, the early active or passive mobilization protocols are not practical for certain patients, such as children and patients with concomitant neurovascular injuries.[8] There are many strategies for tendon treatment currently. Virak et al discovered that ibuprofen, as a non-selective cyclooxygenase inhibitor, can inhibit both COX-1 and COX-2 to control inflammation and prevent tendon adhesion formation.[9] Jiang et al utilized electrospinning technology to construct PELA nanofiber membranes loaded with celecoxib, which can effectively prevent tendon adhesion.[10] Chen et al discovered that inhibiting RelA/p65 in tendons can prevent adhesion formation.[11]

One reason for adhesion formation is oxidative stress induced by inflammatory response following tendon injury. This injury triggers inflammation, which, in turn, leads to hypoxia due to elevated cell metabolism. The resulting cell damage and hypoxia generate free radicals, notably ROS. ROS are a type of oxygen-derived free radicals produced in large amounts by activated leukocytes (neutrophils and macrophages) during inflammatory reactions.[12] Increased production or decreased scavenging of ROS leads to an excess of these free radicals, a condition known as oxidative stress, resulting in lipid peroxidation of plasma membranes, oxidative modification of proteins, DNA damage, and cell death.[13,14] Thus, oxidative stress aggravates cell injury and results in inflammation, while inflammation recruits and activates leukocytes. Active leukocytes produce pro-fibrotic cytokines, such as transforming growth factor β1 (TGF-β1) and platelet-derived growth factor (PDGF), which activate and convert resting fibroblasts into myofibroblasts, resulting in overproduction of collagenous extracellular matrix.[15]

CDs are a new type of zero-dimensional carbon nanomaterials.[16–20] It has recently been shown that CDs-based nanozymes have catalytic activity akin to catalase (CAT) and superoxide dismutase (SOD). CDs may ameliorate inflammatory responses by scavenging ROS.[21–23] To the best of our knowledge, CDs have not yet been investigated for use in tendon surgery applications. Wang et al discovered that UA ameliorated hepatic fibrosis in the rat by specific induction of apoptosis in hepatic stellate cells.[24] Wang et al found that UA decreased oxidative stress, inflammation, and fibrosis in diabetic cardiomyopathy rats.[25] Despite the potential benefits of natural triterpenoid UA, it is rarely used in tendon repair experiments, highlighting a gap in current research. UA's hydrophobic nature and low bioavailability have limited its investigation in tendon repair contexts.[25,26] In this study, for the first time, we synthesized a novel red fluorescent antioxidant carbon dots/ursolic acid co-encapsulated liposomes (RCDs/UA@Lipo) encapsulating the red fluorescent antioxidant carbon dots (RCDs) and UA, in which hydrophobic UA was loaded into the phospholipid bilayer of liposomes, whereas RCDs were placed into the cavity of liposomes. Furthermore, to facilitate local applications, RCDs/UA@Lipo was melted into a photocurable hyaluronic acid methacryloyl hydrogel (HAMA). Our objective was to assess RCDs/UA@Lipo-HAMA's efficacy in reducing tendon adhesion formation and enhancing tendon healing via its anti-oxidative, anti-inflammatory, and anti-fibrotic properties in a rat tendon laceration repair model (Figure 1).

Material and Methods

Preparation and Characterization of the Biomaterials

Preparation of RCDs

RCDs were synthesized via a one-step solvothermal reaction. Initially, 307 mg of glutathione (GSH) (1 mM; Aladdin) and 400 mg of Polyethylene Glycol (PEG) 4000 (Guangfu Reagent) were completely dissolved in 10 mL formamide (Keshi Reagent). This solution was then transferred to a Teflon-lined autoclave and heated at 160°C for 4 hours. After cooling to room temperature, the reaction solution was poured into 30 mL acetone for reverse precipitation, then centrifuged at 10000 rpm for 10 min, and repeatedly washed with acetone 3 times. The final precipitate was dried in an oven at 60°C to obtain RCDs powder for further use.

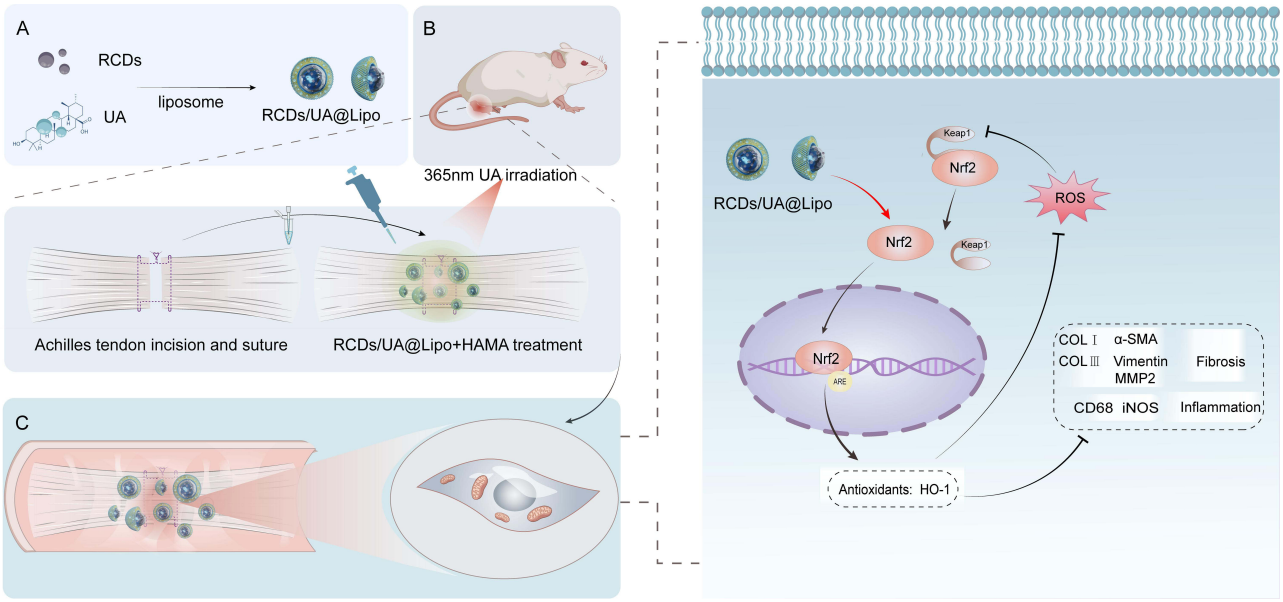

Figure 1 Preparation of RCDs/UA@Lipo-HAMA and schematic diagram of therapeutic mechanisms against adhesion. (**A**) Preparation of RCDs/UA@Lipo for dual-drug co-loading. (**B**) The mixture of RCDs/UA@Lipo and HAMA was precisely applied to the periphery of the sutured tendon model and photocured using 365 nm UV irradiation. This process solidified the HAMA, enabling a localized and sustained release of RCDs and UA. (**C**) RCDs/UA@Lipo-HAMA diminishes oxidative stress by activating Nrf2/HO-1, reducing CD68, and iNOS, and suppressing fibrosis proteins, thereby lessening inflammation and fibrosis, reducing tendon adhesion, and promoting healing.

Preparation of RCDs/UA@Lipo

The RCDs/UA@Lipo were synthesized by a classical hydration method. Briefly, 10 mg UA, 40 mg cholesterol (Macklin), and 160 mg lecithin (Macklin) were dissolved in 20 mL chloroform (Keshi Reagent). A layer of liposome film was obtained by vacuum distillation volatilizing chloroform at 35°C. After that, a layer of liposome film was formed at the bottom of the bottle. Then, 10 mL of 1 mg/mL RCDs PBS solution was prepared and added to hydrate the liposome membrane for 30 min under sonication treatment. Finally, RCDs/UA@Lipo solution was obtained after filtered with a 0.22 μm polyethersulfone filter.

Preparation of RCDs/UA@Lipo-HAMA

The HAMA was first synthesized by an acylation reaction between methacrylic anhydride (Aladdin) and sodium hyaluronate (Yuanye Biotechnology).[27] Then, the working solution of the hydrogel was configured as 20 wt% HAMA and 5 wt% 2-Hydroxy-4'-(2-hydroxyethoxy)-2-methylpropiophenone (Irgacure 2959; Aladdin) that dissolved in 10 mL PBS solution. For RCDs/UA@Lipo-HAMA, an additional 1 mL of the above RCDs/UA@Lipo solution was added to the working solution. When applied, the solution was photocured by irradiating the solution with a 365 nm hand-held Ultraviolet (UV) lamp for 2–3 min immediately after injection.

RCDs and UA Release Experiments

The 10 mL RCDs/UA@Lipo-HAMA working solution was irradiated by a 365 nm portable UV lamp for 2–3 min for light curing, and then the hydrogel was placed in a 50 mL PBS solution. The solution was taken at different intervals for UV-visible spectroscopy measurement, and the characteristic absorption peak intensity at 674 nm was recorded. The absorbances of UA and RCDs were separately converted into the concentrations of UA and RCDs using the concentration-UV absorption intensity curves of UA and RCDs, respectively, and then the release curves of UA and RCDs were separately plotted.

Characterization

Transmission electron microscopy (TEM) images were shot on the Hitachi JEOL JEM-2100 F. UV-Vis absorption spectra were recorded on the Shimadzu 3100 UV-vis spectrophotometer. Photoluminescent spectra (PL) were recorded on the

Shimadzu RF-5301 PC. X-ray photoelectron spectroscopy (XPS) was performed on the ESCALAB 250 spectrometer. The total antioxidant capacity, CAT-like enzyme, and SOD-like enzyme activities were conducted using commercial 2.2'-Azinobis- (3-ethylbenzthiazoline-6-disulfonic acid) (ABTS), CAT, and SOD kit (Beyotime Biotechnology), respectively. According to the instructions, dynamic light scattering (DLS) was performed on the Malvern Zetasizer Pro. Fourier transform infrared spectroscopy (FTIR) was performed on the Nicolet Avatar 360FTIR spectrophotometer. H nuclear magnetic resonance spectra (H NMR) were recorded on the Bruker AVANCE 500 MHz, and scanning electron microscopy (SEM) images were obtained on the Hitachi Regulus 8100.

In vitro Experiments

Cell Culture and Cytotoxicity Assay

NIH/3T3 mouse fibroblast cells (Shanghai Cultured Cell Bank, China) were cultured in DMEM medium (Solarbio, China) with 10% bovine calf serum(Solarbio, China), 100 IU/mL penicillin, and 100 μg/mL streptomycin (Solarbio, China). The cytotoxicity of RCDs/UA@Lipo was tested using the Cell Counting Kit-8 (CCK-8; Servicebio, China). The cells were incubated with RCDs/UA@Lipo (concentration: 1, 2, 4, 6, 8, and 10 μg/mL) for 24 h, and then 10 μL of CCK-8 solution was added (Figure S1). The cells were further incubated at 37°C for 4 h. The optical density was measured using a microplate reader. Mock-treated fibroblasts were used as controls; all other results were normalized to the untreated cells. In the experimental design, we chose 6 μg/mL RCDs/UA@Lipo (the RCDs/UA@Lipo group contains 6 μg/mL UA and 6 μg/mL RCDs) as the concentration for the study, at which the number of viable cells was more than 80%.

Evaluation of Anti-Oxidative Effects of the Biomaterials

NIH/3T3 cells were first incubated with 800μM hydrogen peroxide (H_2O_2) for 0.5 h and then 6 μg/mL of UA@Lipo, RCDs, or RCDs/UA@Lipo was added. The NIH/3T3 cells were divided into five groups: control (untreated), H_2O_2 treatment, H_2O_2+UA@Lipo, H_2O_2+RCDs, and H_2O_2+RCDs/UA@Lipo groups. The cells were further incubated at 37°C for 2 h. The levels of ROS and mitochondrial membrane potential(ΔΨm) were detected using the ROS assay kit (Beyotime, China) and 5, 5', 6, 6'-tetrachloro-1, 1', 3, 3'-tetraethylbenzimidazolylcarbocyanine iodide (JC-1) kit (Beyotime, China) according to the manufacturer's instructions.

Evaluation of Anti-Fibrotic Effects of the Biomaterials

NIH/3T3 cells were incubated with 10 ng/mL TGF-β1 (Peprotech, USA) and 6 μg/mL UA@Lipo, RCDs, or RCDs/UA@Lipo for 24 h. The NIH/3T3 cells were divided into five groups: control (untreated), TGF-β1 treatment, TGF-β1 +UA@Lipo, TGF-β1+RCDs, and TGF-β1+RCDs/UA@Lipo. Following fixation and permeabilization, cells were blocked using 3% bovine serum albumin (BSA) for 1 hour. Incubation proceeded with rabbit anti-mouse antibodies against COL I (1:500; Cat# 91144, CST, USA) and COL III (1:200; Cat#22734-1-AP, Proteintech, USA) and α-SMA (myofibroblast biomarker) (1:200; Cat #19245, CST, USA) at 4°C overnight. CoraLite 488-conjugated goat anti-rabbit antibodies (1:500; Cat# SA00013-2, Proteintech, USA) and CoraLite 594-conjugated goat anti-rabbit antibodies (1:500; Cat# SA00013-4, Proteintech, USA) were used as the secondary antibodies. Cell nuclei were counterstained with 4', 6-diamidino 2-phenylindole (DAPI). Fluorescence images were taken using a confocal microscope(OLYMPUS FV1000, Japan) at a magnification of 400x, and fluorescence intensity was quantified as mean intensity (arbitrary units, a. u. = integrated density/area) using ImageJ software.

Western Blot Analysis

The treated NIH3T3 cells were collected and lysed by RIPA. Nuclear and cytoplasmic fractions were isolated by a nuclear and cytoplasmic protein extraction kit (Beyotime, China). Subsequently, the protein concentrations were quantified by using the BCA protein assay kit (Beyotime, China). The specimens underwent loading and electrophoresis, and then they were transferred onto poly (vinylidene fluoride) (PVDF) membranes. The membranes were blocked with 5% nonfat milk for 1 h at room temperature, the membranes were subsequently exposed to primary antibodies against Nrf2 (1:1000; Cat# 20733, CST, USA), HO-1 (1:1000; Cat#10701-1-AP, Proteintech, USA), β-actin (1:1000; Cat# 4970, CST, USA), GAPDH (1:1000; Cat# 2118, CST, USA) and Histone-3 (1:1000; Cat#ab1791, Abcam, Cambridge, UK) at 4 °C overnight. Next,

the membranes were incubated with secondary antibodies and were developed using ECL detection reagent. Quantification was used by measuring the band intensities' gray values using ImageJ software.

In vivo Experiments

Study Design

This study included 132 male Sprague-Dawley (SD) rats (8 weeks; average weight: 300 g). The animals were accommodated in standard cages and provided food and water ad libitum. The ambient temperature of the housing environment was maintained at 23–25°C. All experimental procedures were performed in accordance with the National Institutes of Health (NIH) guidelines for the care and use of laboratory animals. Rats were randomly divided into six groups: Control (model), Lipo-HAMA (50 μL of 2.5 mg/mL Lipo + 50 μL of HAMA), UA@Lipo-HAMA (50 μL of 2.5 mg/mL UA@Lipo + 50 μL of HAMA), RCDs-HAMA (50 μL of 2.5 mg/mL RCDs + 50 μL of HAMA), RCDs/UA@Lipo-HAMA (50 μL of 2.5 mg/mL RCDs/UA@Lipo + 50 μL of HAMA), and Sham (skin incision without cutting the tendon). The Institutional Review Board of the First Hospital of Jilin University approved the experimental protocol (Approval No. 20230638).

Rat Model of ATI

Under aseptic conditions and general anesthesia with 2.5% isoflurane in oxygen, a 2-cm longitudinal incision was made to expose the Achilles tendon. At 7.5 mm proximal to its insertion, the Achilles tendon was transected and then sutured using a modified Kessler method with 6–0 nylon sutures. Before the incision was closed, the novel biomaterials were meticulously positioned in the targeted area and subsequently solidified in situ by photocuring. This was achieved using a hand-held UV lamp, which emitted light at 365 nm, for a period of 2 to 3 minutes.

Evaluation of Anti-Oxidative and Anti-Inflammatory Effects of the Biomaterials by Immunofluorescent Staining at Two Weeks

To evaluate the expression of Nrf2 and HO-1, key components of the primary anti-oxidative defense system, along with CD68 and iNOS, which are macrophage biomarkers, immunofluorescent staining was conducted on fresh-frozen specimens. (n = 3 per group). The specimens were serially sectioned at a thickness of 5 μm. After permeabilized and blocked, the sections were incubated with rabbit anti-rat antibodies against Nrf2 (1:200; Cat# 80593-1-RR, Proteintech, USA), HO-1 (1:200; Cat#10701-1-AP, Proteintech, USA), CD68 (1:300; GB11067, Servicebio, China), and iNOS (1:200; Cat#18985-1-AP, Proteintech, USA) at 4°C overnight. Secondary antibodies, CoraLite 488-conjugated goat anti-rabbit IgG (1:500; Cat# SA00013-2, Proteintech, USA) and CoraLite 594-conjugated goat anti-rabbit IgG (1:500; Cat# SA00013-4, Proteintech, USA), were applied for visualization. After counterstaining with DAPI, images were captured at a 400-fold magnification. The amount of fluorescence was quantified by measuring the mean intensity (a. u). (= integrated density/area) using the ImageJ software.

Evaluation of Anti-Fibrotic Effects of the Biomaterials by Immunofluorescent Staining at Six Weeks

The fresh tissue sections were incubated with rabbit anti-rat antibodies against COL III (1:200; Cat#22734-1-AP, Proteintech, USA) and α-SMA (1:200; Cat#19245S, Cell Signaling Technology, USA) at 4°C overnight. CoraLite 488-conjugated goat anti-rabbit IgG (1:500; Cat# SA00013-2, Proteintech, USA) and CoraLite 594-conjugated goat anti-rabbit IgG (1:500; Cat# SA00013-4, Proteintech, USA) were used as the secondary antibodies.

Evaluation of Anti-Fibrotic Effects of the Biomaterials by Immunohistological Staining at Six Weeks

After fixation and embedment, the tissue sections were incubated with rabbit anti-rat antibodies against Vimentin (fibroblast biomarker; 1:3000; Cat#10366-1-AP, Proteintech, USA), α-SMA (1:5000; Cat#14395-1-AP, Proteintech, USA), and MMP2 (1:200; Cat#10373-2-AP, Proteintech, USA) at 4°C overnight. Horseradish peroxidase-labeled goat anti-rabbit IgG was used as the secondary antibody. Staining was visualized with 3, 3′-diaminobenzidine (DAB) and hematoxylin. The amount of positive staining was measured by average optical density (OD) (a. u). (= integrated density/area) using the ImageJ software.

Evaluation of Adhesion Formation at 2, 4, and 6 Weeks

Hematoxylin and eosin staining (H&E staining) tissue sections from the tendon-skin interface were used to assess the tendon adhesion formation of ATI. The tendon and its overlying skin were harvested en bloc, without the tibia (n = 3 per group). After fixation, embedment, dehydration, and deparaffinization, the specimens were longitudinally sectioned into 5μm slices and stained with H&E. Under a light microscope (40 ×), the degree of adhesion formation was scored in a blinded manner by two independent examiners, according to the scoring criteria of Tang.[28] The average scores for each section were used for the data analysis. To detect collagen type at the site of tendon repair, the sections were stained with Sirius red (Solarbio, Beijing, China) and observed under a polarized light microscope (200×; OLYMPUS, Tokyo, Japan).

Evaluation of Locomotor Activity at 2, 4, and 6 Weeks

The locomotor activity of the rats was evaluated by Achilles functional index (AFI) in an established experiment.[29] Briefly, black ink was placed on the feet of the rats to analyze the walking pattern revealed by footprints on paper. The measured parameters included the print length (PL), the width of toe spreading (TS) (= the distance between the first and fifth toes), and the width of intermediate toe spreading (IT) (= the distance between the second and fourth toes). Based on these parameters, the factors were calculated as follows: PLF = (PL of normal hindpaw – PL of injured hindpaw)/ PL of injured hindpaw; TSF = (TS of injured hindpaw – TS of normal hindpaw)/TS of normal hindpaw; ITF = (IT of injured hindpaw – IT of normal hindpaw)/IT of normal hindpaw. The AFI was calculated by the following formula: AFI = 74×PLF + 161×TSF + 48 ×ITF – 5. AFI score of 0 indicates normal motor function, while scores below 0 indicate impaired motor function, with −100 representing a complete loss of motor function.

Evaluation of Tendon Healing at 2, 4, and 6 Weeks

The quality of tendon healing at the tendon repair site was evaluated by maximal failure force on a universal testing machine (Instron 5568, USA). Along the original incision, the Achilles tendon was dissected out and transected at the musculotendinous junction. The hindpaw including the insertion of the Achilles tendon was preserved. Prior to testing, the skin and tibia were resected, and the specimens were kept moist in saline-soaked gauze. The preload was 0.01 N (Newton) and the loading rate was 10 mm/min. The maximal failure force, expressed in Newtons (N), was determined by the load at which the tendon repair site failed.

Rat Model of FDPI

Under aseptic conditions and with the animal under general anesthesia, a 1.5-cm longitudinal incision was made in the plantar aspect of the right foot. Initially, the flexor digitorum superficialis tendon (FDS) was carefully exposed and subsequently resected to reveal the underlying flexor digitorum profundus (FDP). The FDP tendon was transected and then sutured using a modified Kessler method with 6–0 nylon sutures. Before skin closure with 4–0 sutures, the biomaterials were implanted and photocured by irradiation with a 365 nm hand-held UV lamp for a duration of 2 to 3 minutes.

Evaluation of Tendon Gliding at Six Weeks

The effects of the biomaterials on tendon gliding after tendon repair were evaluated in the rat model of the FDPI, using an established method.[30] The rats were anesthetized with 2.5% isoflurane in oxygen. Along the original skin incision, the FDP tendon was dissected out and transected at its musculotendinous junction. Then the hindpaw was amputated 5 mm proximal to the ankle. With a 1mL syringe needle, the hindpaw was fixed in a foam board without restricting tendon gliding. The proximal end of the FDP tendon was connected to different weights (5, 10, 15, and 20 g) with silk sutures, ensuring the toes remained in full extension. The flexion of the toes was controlled by weight. The angle of flexion of the toes depended on the degree of tendon adhesion and the different weights. The angle of flexion of the longest toe was captured by a digital camera and measured by the ImageJ software.

Statistical Analysis

Statistical analyses were conducted using IBM SPSS Statistics version 25(IBM, USA) and GraphPad Prism 9.5 (GraphPad Software, USA). Data normality was tested using the Shapiro–Wilk test. Data conforming to normal distribution were expressed as mean ± standard deviation (SD). Comparisons between the groups were analyzed with one-way analysis of variance (ANOVA), two-way ANOVA, and repeated-measures ANOVA, with post-hoc analysis conducted through Tukey's test for multiple comparisons. (ns, no significant; * $p < 0.05$; ** $p < 0.01$; *** $p < 0.001$; **** $p < 0.0001$).

Results

Characterization and Anti-Oxidative Properties of RCDs

As shown in Figure 2A, the transmission electron microscopy (TEM) image of RCDs showed that they were uniformly dispersed nanoparticles with an average size of 2.5 nm (Figure 2B). Such ultra-small size was conducive to the efficient entry of RCDs into cells to exert antioxidant effects. It could be seen that the greenish aqueous solution of RCDs could emit red fluorescence under ultraviolet light excitation (inset of Figure 2C). The photoluminescent (PL) spectra appeared a maximum emission peak at 681 nm and several excitation peaks at 420, 628 and 676 nm, corresponding to the UV-Vis absorption spectra of RCDs (Figure 2C). Under excitation light irradiation in the range of 550 to 600 nm, RCDs could produce intensity-dependent red fluorescence, suggesting the bioimaging potential of RCDs (Figure 2D). The X-ray photoelectron spectroscopy (XPS) indicated four elements within the RCDs, namely, C, N, O, and S, consistent with the precursors (Figure 2E). The atomic ratio was calculated as 51.2%, 22.3%, 24.0%, and 2.5% for C, N, O, and S, respectively, according to the peak area of XPS. The deconvoluted C 1s spectra of RCDs contained four types of C bonding forms, namely sp^2/sp^3 C (C-C/C=C), C-S/C-N/C-O, C=S/C=N/C=O, and amide bond (N-C=O) (Figure 2F), indicating the graphite carbon core and surface functional groups that containing S, N, and O. There were four kinds of S bonding forms showing in the S 2p spectra, which were thiol, COSH, C-S, and S=O, confirming the S doping within RCDs (Figure 2G). The N 1s and O 1s spectra also determined the existence states of pyridine/pyrrolic N and single/double bond O (Figure S2).

RCDs significantly reduced the production of ABTS cationic free radicals in a concentration-dependent manner (Figure 2H). At the same mass concentration, RCDs exhibited an anti-oxidative effect similar to Trolox on glutathione (GSH). Although RCDs did not catabolize H_2O_2, RCDs efficiently decomposed superoxide anion radicals ($\bullet O_2^-$) at very low concentrations (Figure 2I and J). Cell imaging showed that the cells presented red fluorescence of RCDs after 2 h of co-culture, indicating rapid entry of RCDs into the cells (Figure 2K and L).

Characterization of RCDs/UA@Lipo

RCDs/UA@Lipo exhibited characteristic absorption peaks of UA and RCDs (Figure S3). After loaded with UA and RCDs, the size of liposomes increased (inset of Figure 3A). Dynamic light scattering (DLS) showed that the average sizes were 76.6, 110.1, and 137.5 nm for liposome (Lipo), UA@Lipo, and RCDs/UA@Lipo, respectively (Figure 3A). Fourier transform infrared spectroscopy (FTIR) demonstrated that RCDs/UA@Lipo contained the characteristic vibration absorption peaks of UA and RCDs (Figure 3B). The H nuclear magnetic resonance spectra (H-NMR) showed that HAMA appeared two new signals at 5.6 and 6.2 ppm compared with hyaluronic acid (HA), which corresponded to the -$CH{=}CH_2$ group (Figure S4). The solution of RCDs/UA@Lipo-HAMA was an injectable liquid state; 2 min of irradiation with a hand-held 365 nm UV lamp solidified RCDs/UA@Lipo-HAMA into a gel state (Figure 3C). Scanning electron microscopy (SEM) showed that the gel state of RCDs/UA@Lipo-HAMA was a loose and porous structure (Figure 3D). Compared with HAMA, white spots appear on the porous mesh layer of RCDs/UA@Lipo-HAMA (indicated by the black arrows), which may suggest the presence of nanoparticles in the hydrogel (Figure S5).

In vitro UA and RCDs Release of RCDs/UA@Lipo

RCDs/UA@Lipo-HAMA gel was soaked in PBS and sampled regularly (Figure S6). The amount of UA released from the RCDs/UA@Lipo-HAMA gel was calculated according to the relationship curve between the mass concentration and UV absorption intensity of UA (Figure 3E) (Figure S7). The amount of UA released was approximately 50% on the

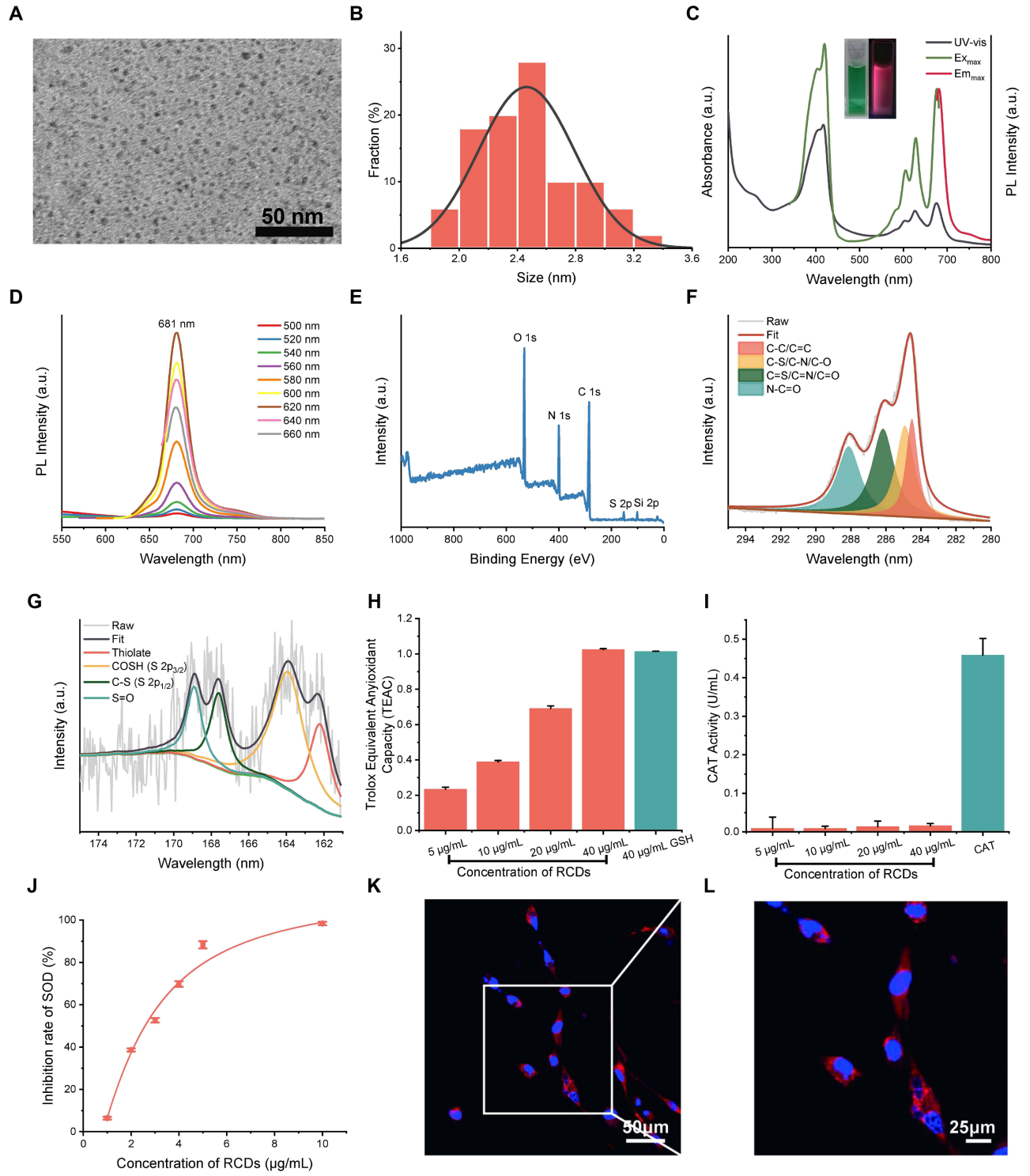

Figure 2 Characterization of RCDs. (**A**) TEM image of RCDs. (**B**) Size distribution histogram of RCDs. (**C**) UV-Vis absorption and maximum excitation/emission PL spectra of RCDs (inset shows the photographs of RCDs solution under daylight and UV light). (**D**) PL spectra of RCDs under different excitation wavelengths. (**E**) XPS spectra of RCDs. (**F**) Deconvoluted C1s spectra and (**G**) S 2p spectra of RCDs. (**H**) Antioxidant capacity assay of RCDs by ABTS method. (**I**) CAT-like activity assay of RCDs. (**J**) SOD-like activity assay of RCDs. (**K**) and (**L**) Cell imaging of RCDs under different magnifications.

first day and then slowed down and reached a plateau at 4 days. Ultimately, approximately 80% of the UA was released from the RCDs/UA@Lipo-HAMA gel. Based on the UV absorbance-concentration curves of UA and RCDs (Figure S8), the loading capacity of Lipo for RCDs and UA is 27.8% and 72.3%, respectively. The in vitro release behavior of RCDs

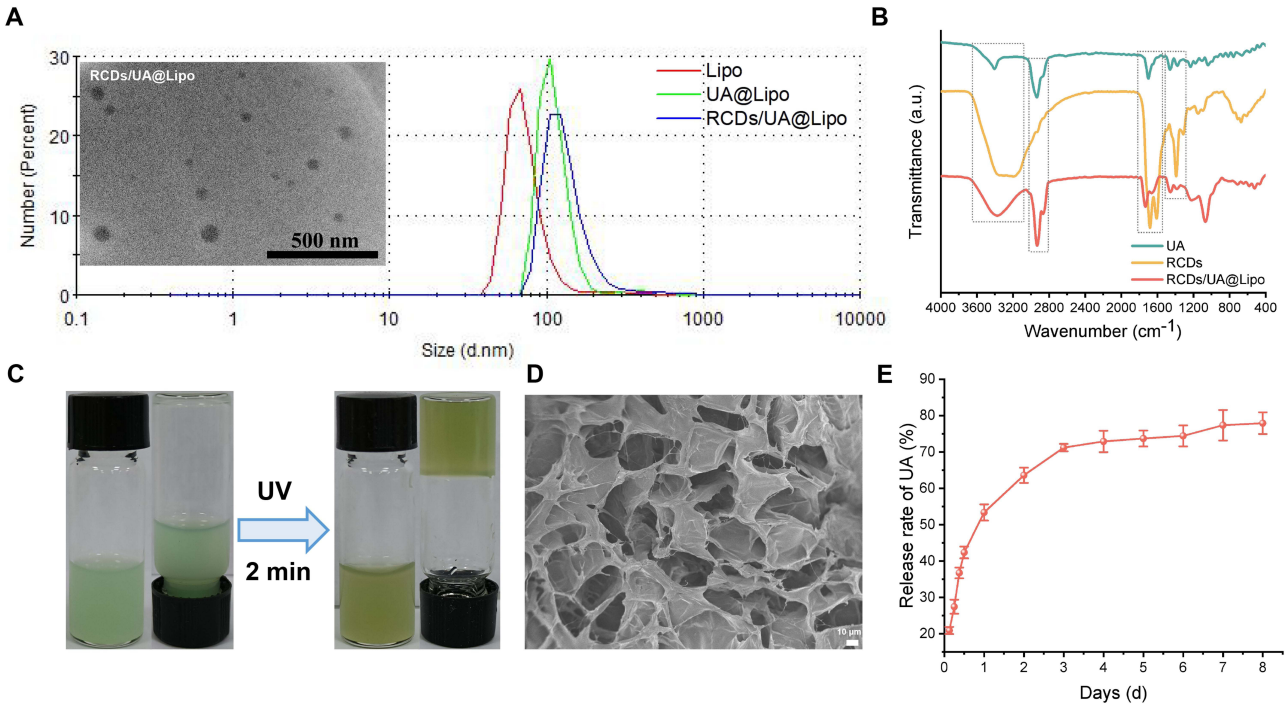

Figure 3 Characterization of RCDs/UA@Lipo-HAMA. (**A**) Particle size distribution curve of Lipo, UA@Lipo, and RCDs/UA@Lipo (inset shows the typical TEM image of RCDs/UA@Lipo). (**B**) FTIR spectra of UA, RCDs, and RCDs/UA@Lipo. (**C**) Photographs of RCDs/UA@Lipo-HAMA before and after UV irradiation for 2 min. (**D**) SEM image of the internal structure of RCDs/UA@Lipo-HAMA after photocuring. (**E**) Release curve of UA from RCDs/UA@LipoHAMA.

from RCDs/UA@Lipo-HAMA had been elucidated by monitoring the change of fluorescence intensity in the supernatant after being immersed in PBS at different times. As shown below, it could be seen that RCDs had a sudden release in the first 4 h, and then reached a stable period. About 80% of RCDs were released in about 6 h (Figure S9). This was because RCDs had excellent water solubility, so they followed different release kinetics from insoluble UA, which was also in line with our design of early anti-oxidation by RCDs, and subsequently inhibition of fibrosis adhesion by UA.

RCDs/UA@Lipo Exhibited Anti-Oxidative and Anti-Fibrotic Effects in the Cell Models

To investigate the anti-oxidative effects of the biomaterials, we used H_2O_2 to stimulate mouse fibroblasts. Compared with the control group (untreated fibroblasts), the stimulation of H_2O_2 significantly increased ROS level (H_2O_2:1.00 ± 0.04 vs Control: 0.123 ± 0.03; $p < 0.001$), whereas UA@Lipo, RCDs, or RCDs/UA@Lipo significantly reduced ROS in mouse fibroblasts stimulated by H_2O_2 (UA@Lipo: 0.572 ± 0.06; RCDs: 0.690 ± 0.08; RCDs/UA@Lipo: 0.449 ± 0.06) ($n = 3$; $p < 0.001$) (Figure 4A and D). Mitochondria are major sites of intracellular ROS production. The stimulation of H_2O_2 significantly devastated mitochondrial membrane potential (H_2O_2: 1.00 ± 0.04 vs Control: 0.701 ± 0.01; $p < 0.001$), whereas UA@Lipo, RCDs, or RCDs/UA@Lipo significantly recovered mitochondrial membrane potential in mouse fibroblasts stimulated by H_2O_2 (UA@Lipo: 0.814 ± 0.01 vs. H_2O_2; $p < 0.001$) (RCDs: 0.796 ± 0.03 vs H_2O_2; $p < 0.001$) (RCDs/UA@Lipo: 0.569 ± 0.01 vs H_2O_2; $p < 0.001$) ($n = 3$) (Figure 4B and E).

To assess the anti-fibrotic effects of biomaterials, we used TGF-β1 to stimulate mouse fibroblasts. The stimulation of TGF-β1 significantly increased the expression of collagen proteins and α-SMA (COL I: TGF-β1:2.743 ± 0.58 vs Control: 1.00 ± 0.28; $p = 0.001$) (COL III: TGF-β1:1.632 ± 0.20 vs Control: 1.00 ± 0.08; $p = 0.004$) (α-SMA: TGF-β1: 1.516 ± 0.07 vs 1.00 ± 0.18; $p = 0.006$), whereas RCDs/UA@Lipo significantly decreased the expression in mouse fibroblasts stimulated by TGF-β1 (COL I: 0.694 ± 0.15 vs TGF-β1; $p < 0.001$) (COL III: 1.018 ± 0.25 vs TGF-β1; $p = 0.005$) (α-SMA: 0.888 ± 0.20 vs TGF-β1; $p = 0.002$) (Figure 4C, F-H).

To verify that RCDs/UA@Lipo exerts its antioxidative effects by activating the NRF2/HO-1 signaling pathway, we conducted WB and IF experiments (Figure S10 and S11). We found that the expression of NRF2 in the nucleus was

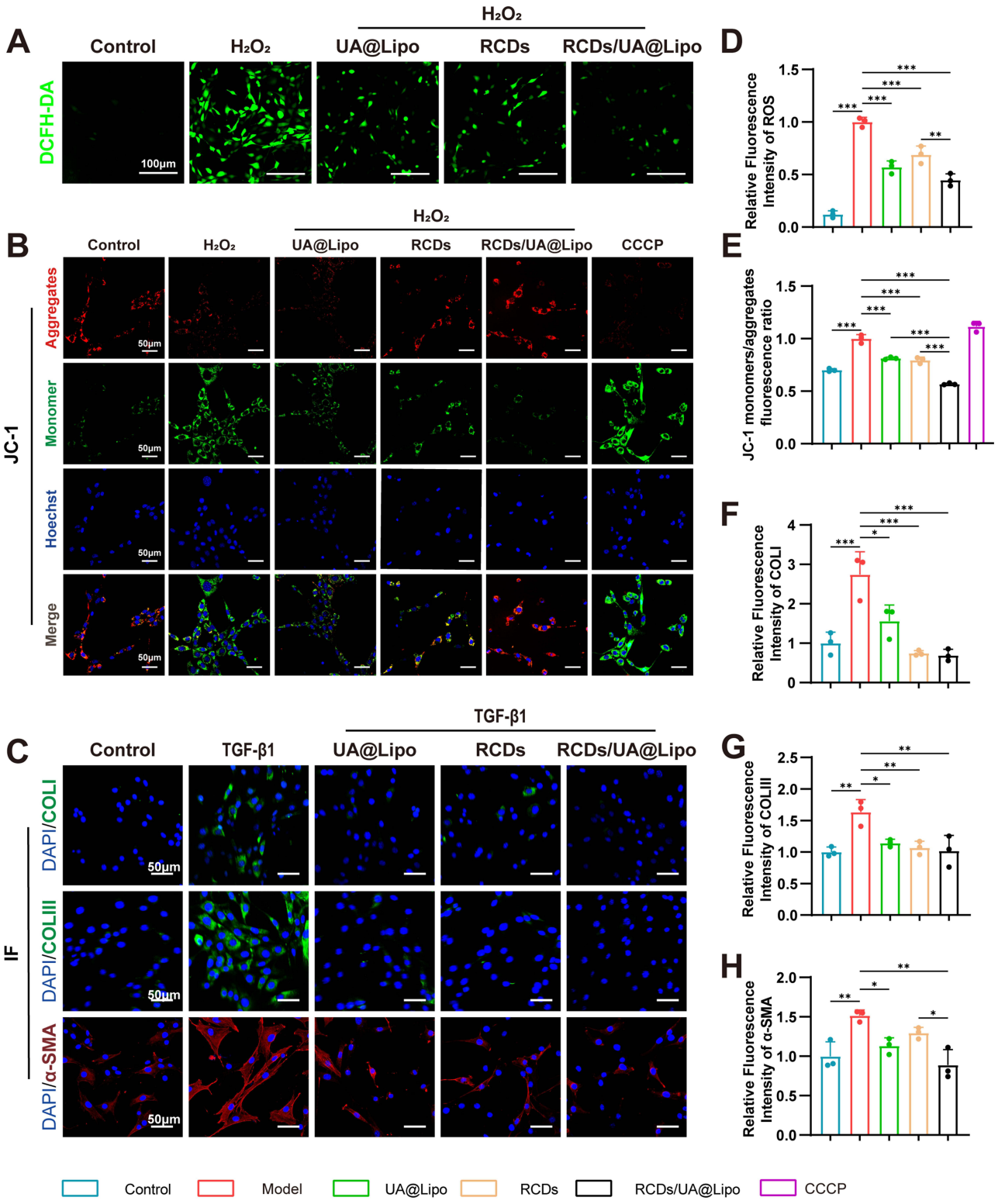

Figure 4 RCDs/UA@Lipo alleviated H_2O_2-induced oxidative stress and TGF-β1 induced fibrosis-specific markers separately. (**A**) Immunofluorescence staining images of intracellular ROS and superoxide detected by DCFH-DA probe. (**B**) mitochondrial membrane potential (ΔΨm) detected by JC-1 probe. (**C**) tendon fibrosis markers (COL I, COL III, α-SMA) of NIH3T3. (**D–H**) Semiquantitative analysis of the relative fluorescent intensity of (**A–C**) (n = 3). (**D** and **E**) Model group is H_2O_2 group, (**F–H**) Model group is TGF-β1 group. Data are presented as mean ± SD; comparisons between the groups were performed one-way ANOVA. *P < 0.05; **P < 0.01; ***P < 0.001.

significantly higher in the RCDs/UA@Lipo group compared to other groups, while the expression of NRF2 in the cytoplasm was significantly lower. Additionally, the expression of HO-1 protein was also significantly increased. This indicates that RCDs/UA@Lipo promotes the translocation of NRF2 into the nucleus, thereby initiating the expression of the antioxidant gene HO-1. (Figure S10). The mechanism of action of ML385 primarily involves the direct inhibition of NRF2 binding to the promoter regions of its target genes. This binding typically occurs through antioxidant response elements (ARE). By blocking this interaction, ML385 can inhibit the transcriptional activity of NRF2, thereby reducing the expression of antioxidant and other metabolic genes.[31,32] Conversely, the Nrf2 inhibitor ML385 (1 μM) significantly abrogated the effects of RCDs/UA@Lipo on the protein levels of Nrf2 and HO-1 activity. Compared with the H_2O_2+RCDs/UA@Lipo group, the expression of NRF2 and HO-1 was decreased in the H_2O_2+RCDs/UA@Lipo+ML385 group. Additionally, ML385 inhibited the beneficial effects of RCDs/UA@Lipo on intracellular ROS and superoxide (Figure S11). Through a rescue experiment, we confirmed that RCDs/UA@Lipo exerts its antioxidative effects by activating NRF2.

RCDs/UA@Lipo-HAMA Exhibited Anti-Oxidative, Anti-Inflammatory, and Anti-Fibrotic Effects in the ATI

To investigate the biofunctionality of the biomaterials, their biosafety was first evaluated by histological analysis and serological test at 6 weeks after biomaterial implantation. No damage was observed in the heart, liver, spleen, lung, and kidney (Figure 5A). No increase in serologic markers such as AST, ALT, TP, and CREA was observed compared with untreated rats (Figure 5B). In addition, the rats treated with the biomaterials did not show any signs of toxicity, such as weight loss, reduced activity, or ruffled fur; no inflammatory signs were observed in the skin incision.

The effects of biomaterials on adhesion formation were evaluated in the rat model of ATI (Figure 6A). Gross examination revealed that the injured tendons were thicker than the intact tendons (sham group) at 2, 4, and 6 weeks. However, the tendons in the RCD/UA@Lipo-HAMA group were thinner than those in the other groups at 6 weeks (Figure 6B). To assess the anti-oxidative and anti-inflammatory effects of the biomaterials, we detected the expression of Nrf2/HO-1(prime anti-oxidative defense system), CD68 and iNOS (macrophage biomarker) by immunofluorescent staining 2 weeks after tendon repair. Compared with the control group, the expression of Nrf2 and HO-1 in the RCDs/UA@Lipo-HAMA group was significantly increased ($p < 0.001$), whereas the expression of CD68 and iNOS was significantly decreased ($p < 0.001$) (Figure 6C, F-I). To evaluate the anti-fibrotic effects of the biomaterials, we detected the expression of COL III, α-SMA, Vimentin, and MMP2 6 weeks after tendon repair. Immunofluorescent staining showed that, compared to the control group, RCDs/UA@Lipo-HAMA significantly reduced the expression of COL III ($p = 0.002$) and α-SMA ($p < 0.001$). Immunohistochemical staining showed that, compared to the control group, RCDs/UA@Lipo-HAMA significantly decreased the expression of Vimentin ($p < 0.001$), MMP2 ($p < 0.001$), and α-SMA ($p < 0.001$) (Figure 6D, E and J–N).

RCDs/UA@Lipo-HAMA Attenuated Adhesion Formation After the ATI

H&E staining was performed to investigate the effects of RCDs/UA@Lipo-HAMA on adhesion formation following ATI. Gross examination revealed a dense scar between the tendon and its overlying skin in the control group, whereas a gap was observed between the tendon and its overlying skin after biomaterial implantation (Figure 7A). By quantifying adhesion formation according to the scoring criteria proposed by Tang[28] (Figure 7B), the degree of adhesion formation was compared among groups at 2, 4, and 6 weeks after biomaterial implantation using two-way ANOVA ($n = 3$). The results showed that the interaction between grouping and time points was not significant ($F = 0.492$; $p = 0.808$). Thus, the main effects were tested. The main effect of grouping was significant ($F = 17.88$; $p < 0.001$), where the adhesion score for the RCDs/UA@Lipo-HAMA group was significantly lower than that for the other groups. The main effect of time points was also significant ($F = 14.47$; $p < 0.001$), where the adhesion scores at 4 weeks and 6 weeks were significantly lower than those at 2 weeks. Multiple comparisons using Tukey's test indicated that the adhesion score for the RCDs/UA@Lipo-HAMA group was lowest at 6 weeks. Sirius Red staining showed that the collagen fibers were regularly aligned, and COL I was predominant at the site of tendon repair in the RCDs/UA@Lipo-HAMA group (Figure 7C).

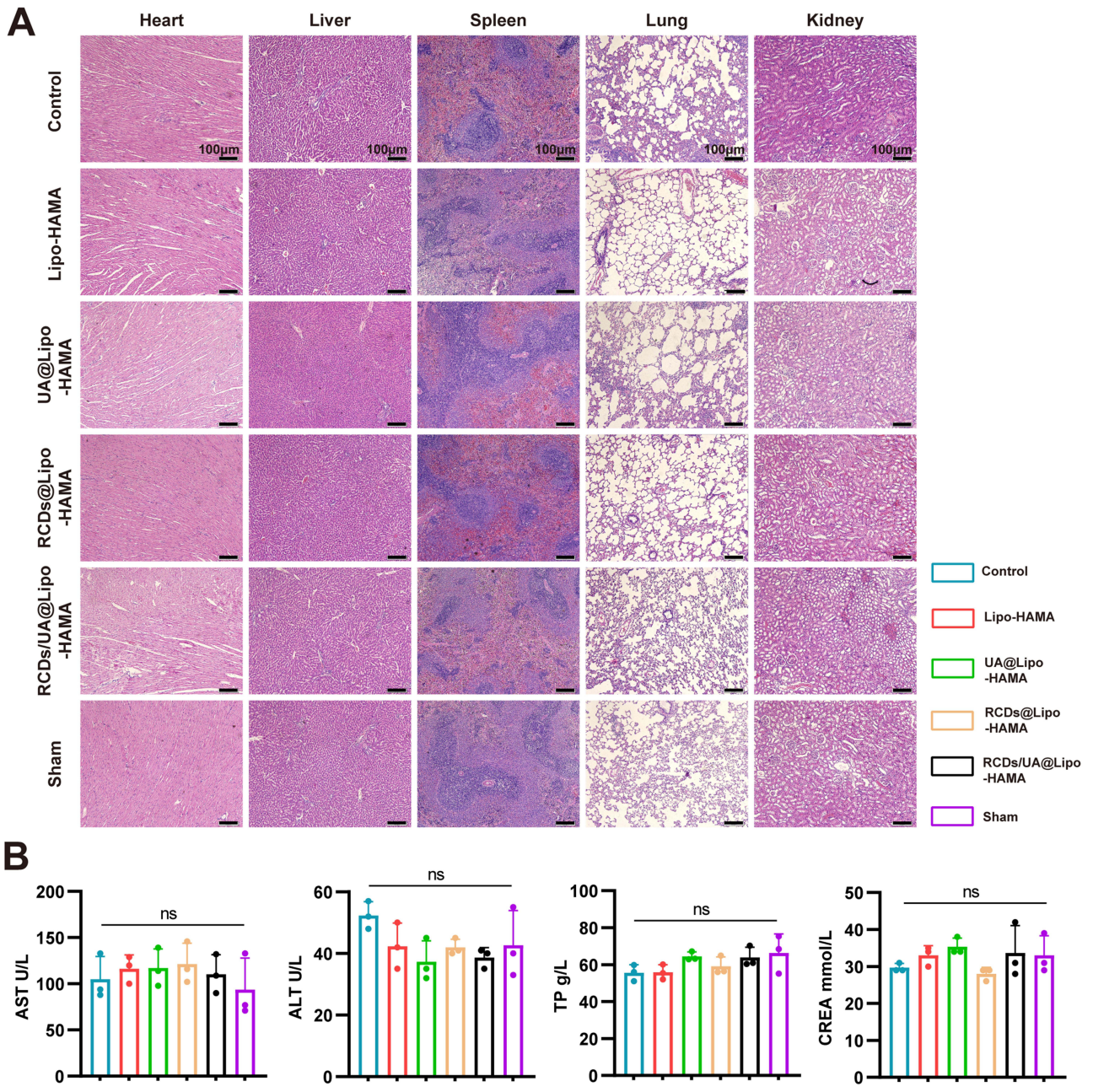

Figure 5 Verification of biological safety of different groups in vivo. (**A**) Morphology of the major function organ (heart, liver, spleen, lung, and kidney) at 6 weeks postoperatively (n = 3). (**B**) Blood biochemistry tests at 6 weeks postoperatively (n = 3). AST, aspartate transaminase; ALT, alanine aminotransferase; TP, total protein; CREA, creatinine. Data are presented as mean ± SD. ns, no statistical significance.

RCDs/UA@Lipo-HAMA Improved Motor Function After the ATI

The motor function of rats with ATI was quantified by the AFI (Figure 7D and E). Repeated-measures ANOVA(n = 4) was performed to compare the differences in AFI among the groups. The assumption of sphericity was verified using Mauchly's test and the Bonferroni method was used to perform pairwise comparisons. Mauchly's test revealed that the assumption of sphericity was plausible ($p = 0.870$). There was a significant interaction between grouping and time points ($p = 0.012$), suggesting that AFI across the three-time points (2, 4, and 6 weeks) was dependent on grouping. The overall test results for the differences in AFI were significant ($p < 0.001$). Pairwise comparisons indicated that the AFI for the RCDs/UA@Lipo-HAMA group was significantly better than that for the Lipo-HAMA group ($p < 0.05$), the UA@Lipo-HAMA group ($p = 0.005$), the RCDs-HAMA group ($p < 0.001$), and the control group ($p < 0.001$).

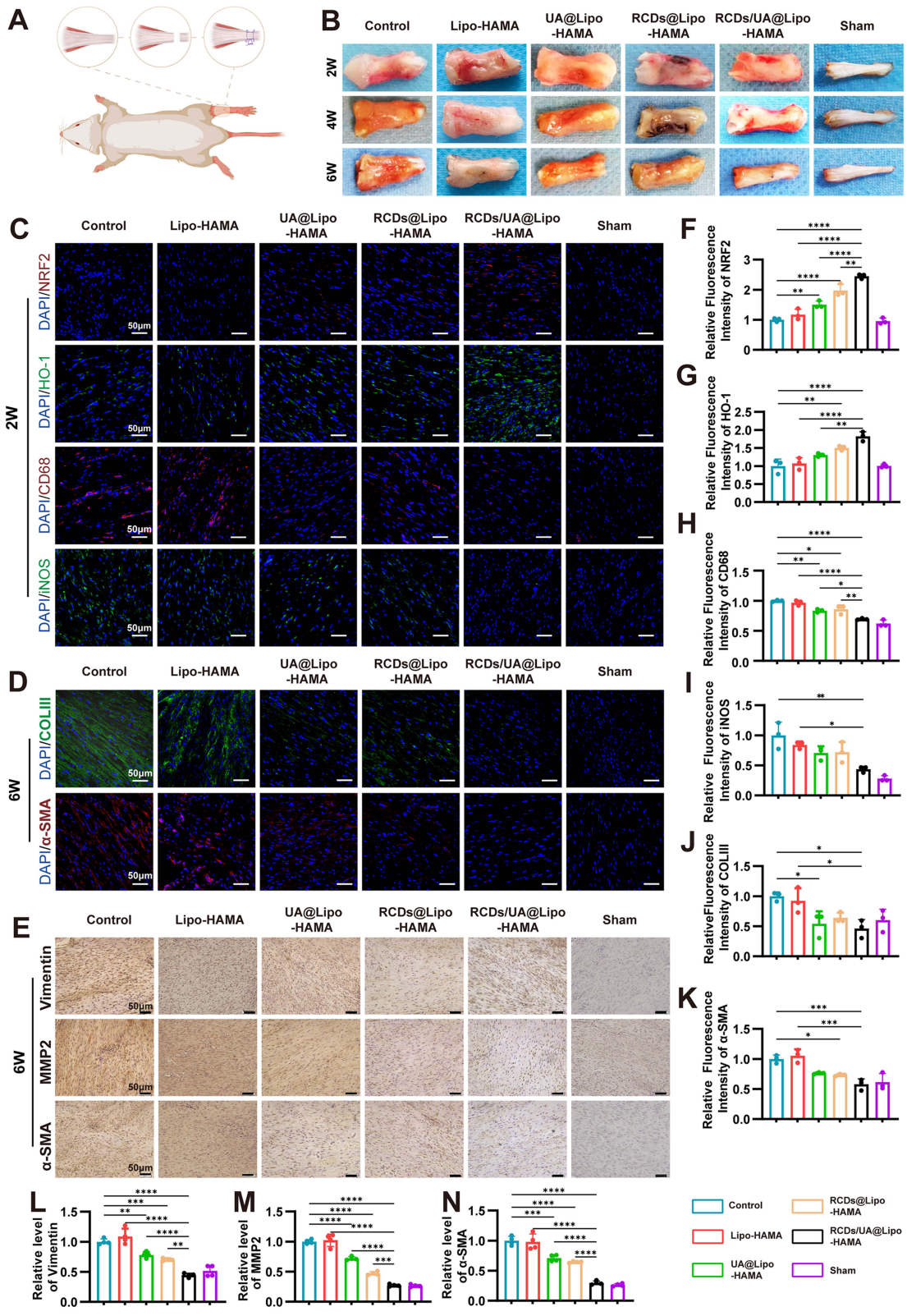

Figure 6 RCDs/UA@Lipo-HAMA reduced adhesion of injured tendons at macroscopic and histological levels at various time points post-injury. (**A**) Schematic diagram of surgical procedures of the ATI. (**B**) Gross view of ATI. (**C**)Representative images of immunofluorescence staining of tendon antioxidant (Nrf-2, HO-1) and anti-inflammatory markers (CD68, iNOS) at 2 weeks post-injury (n = 3). (**D**) Representative images of immunofluorescence staining of tendon antifibrosis (COL III, α-SMA) at 6 weeks post-injury (n = 3). (**E**) Representative images of immunohistochemical staining of tendon markers (Vimentin, MMP2, α-SMA) antifibrosis at 6 weeks post-injury (n = 4). (**F–N**) Semiquantitative analysis of expression level of tendon marker of (**C–E**), respectively. Data are presented as mean ± SD; comparisons between the groups were performed by one-way ANOVA. *P < 0.05; **P < 0.01; ***P < 0.001; ****P < 0.0001.

https://doi.org/10.2147/IJN.S466312 DovePress

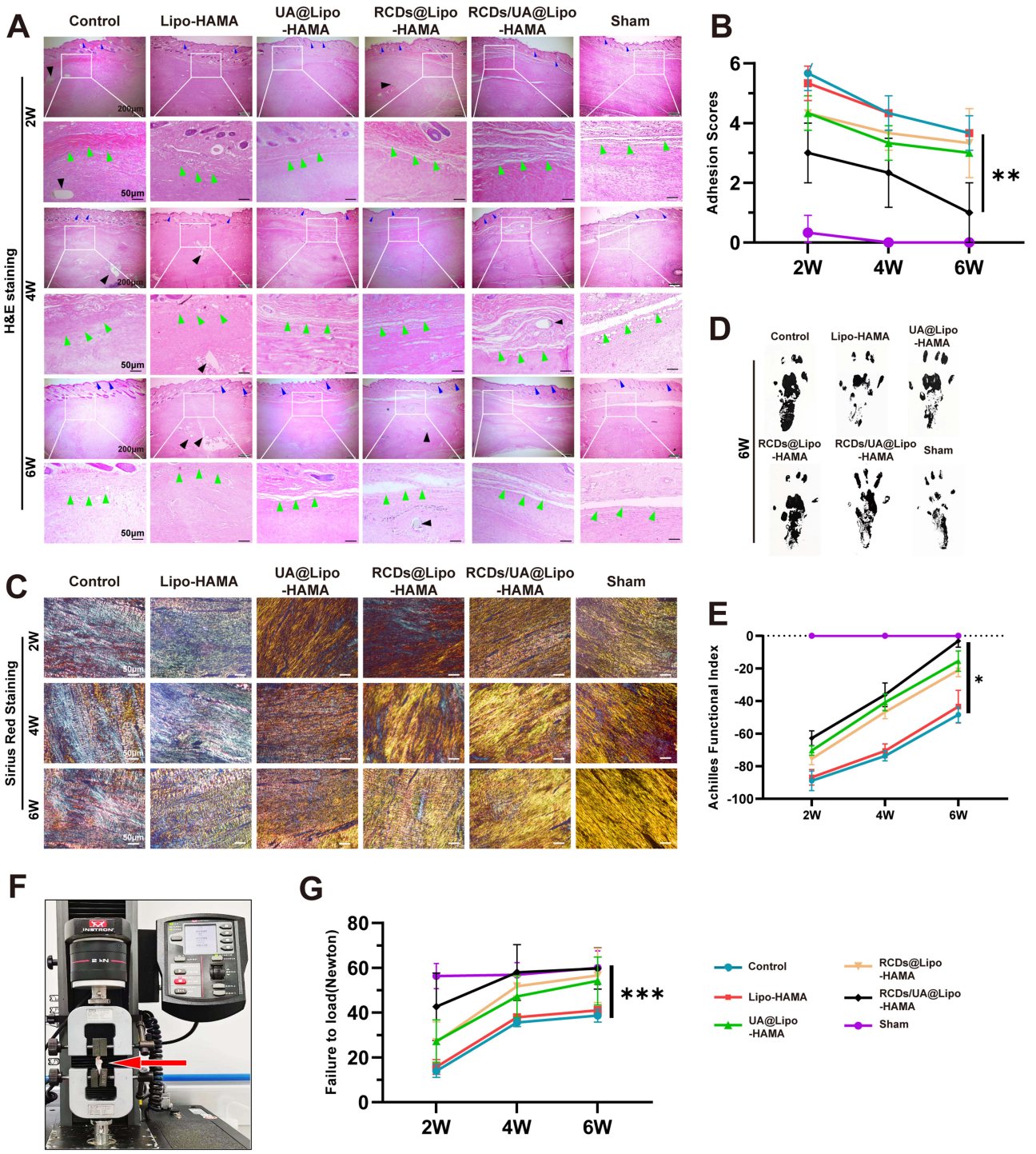

Figure 7 RCDs/UA@Lipo-HAMA restored histological changes and functions of the Achilles tendon. (**A**) Representative images of H&E staining (n = 3). Green arrow: interfaces between the skin and injured tendon. Blue arrow: skin. Black arrow: suture. (**B**) Adhesion Scores evaluate. (**C**) Representative images of Sirius Red staining (n = 3). (**D**) Footprints and (**E**) Achilles Functional Index (AFI) of rats from different groups at various times postinjury (n = 4). (**F**) Images of the dynamometer. (**G**) Biomechanical properties of the regenerated tendons failure force (n = 3). Comparisons between the groups were performed by two-way ANOVA and repeated measures ANOVA. *P < 0.05; **P < 0.01; ***P < 0.001.

RCDs/UA@Lipo-HAMA Improved Tendon Healing

The healing quality of the ATI was quantified by maximal failure force (Figure 7F and G). Two-way ANOVA (n = 3) was performed to determine whether there was a difference in the maximal failure force among the groups at different time points. The results showed that there was no significant interaction (p = 0.268). The main effect for different time points

(2, 4, and 6 weeks) was significant ($p < 0.001$), where it was seen that maximal failure force increased over time. The main effect of grouping was also significant ($p < 0.001$). Multiple comparisons using Tukey's test indicated that the maximal failure force significantly increased in the RCDs/UA@Lipo-HAMA group, the RCDs-HAMA group, and the UA@Lipo-HAMA group compared with the control group ($p < 0.001$, $p = 0.006$, and $p = 0.021$, respectively). In addition, no significant difference was found between the RCDs/UA@Lipo-HAMA group and the sham group (normal tendons) ($p = 0.830$).

RCDs/UA@Lipo-HAMA Improved Tendon Gliding After the FDPI

The FDP tendon belongs to intrasynovial tendons, which are susceptible to adhesion formation.[30] To assess the effect of the biomaterials on adhesion formation, the gliding function after FDPI repair was evaluated by measuring the angle of flexion of the longest toe(Figure 8A–C). The comparison among groups at different weights was performed by repeated measures ANOVA (n = 4). Mauchly's test revealed that the assumption of sphericity was plausible ($p = 0.948$). For the interaction between groups and weights, the test indicated that this interaction was statistically significant ($p = 0.003$), suggesting that the angle of flexion of the toe made across the five weights was dependent on the type of treatment groups. Post hoc Scheffé multiple comparisons indicated that the control group made the least angle of flexion (mean = 21.21°), with the Lipo-HAMA group, the UA@Lipo-HAMA group and the RCDs-HAMA group making more angle of flexion (mean =22.79°; 26.82°; 28.14°, respectively; $p = 1.000$), and the sham group and the RCDs/UA@Lipo-HAMA group making the most angle of flexion (mean = 37.65°; 34.32°; $p = 0.199$), averaged across the four trials.

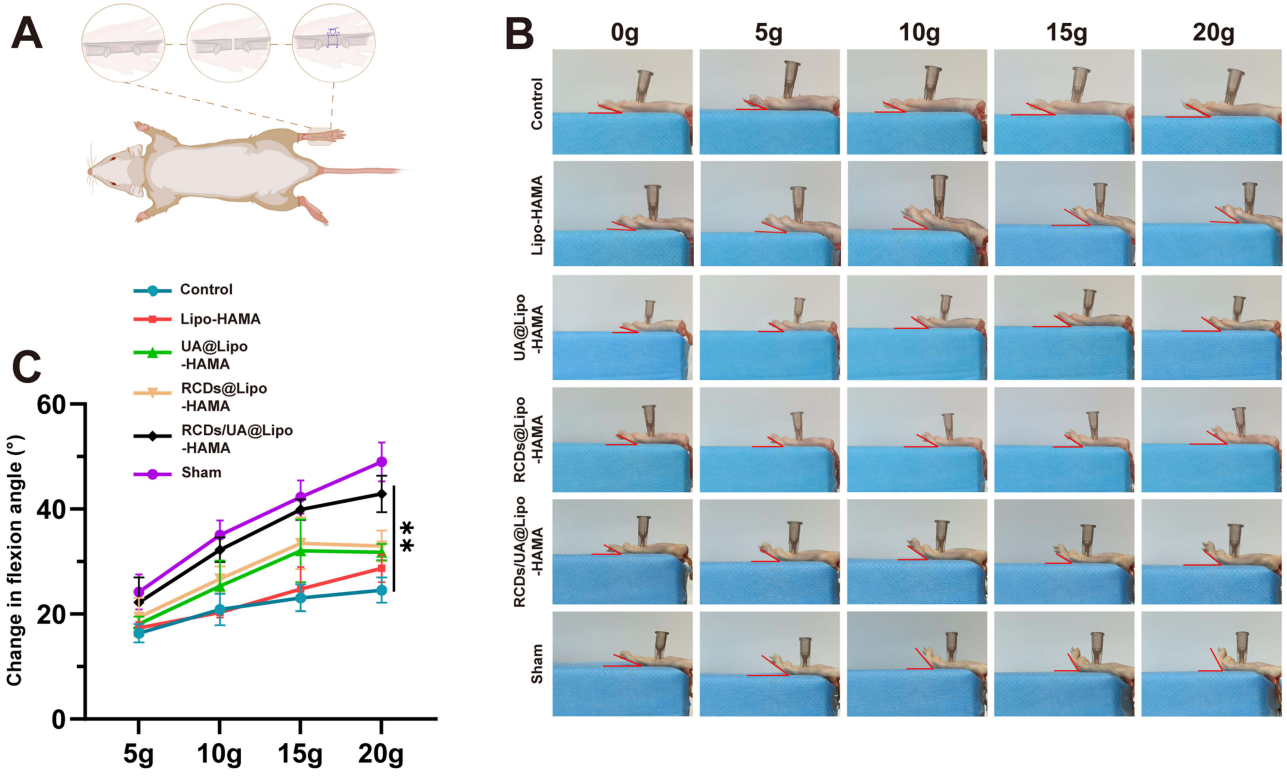

Figure 8 RCDs/UA@Lipo-HAMA improved tendon gliding after FDPI. (**A**) Schematic diagram of surgical procedures of FDPI. (**B**) Typical images of the flexion angle of tendons in different groups at 0, 5, 10, 15, and 20 g at 6 weeks. (**C**) The analysis of flexion angle change of repaired tendons (n = 4). Comparisons between the groups were performed by repeated-measures ANOVA. **P < 0.01.

Discussion

The formation of adhesions between injured tendons and surrounding tissues, which affects tendon function recovery, is a significant challenge in orthopedic clinical practice.[33,34] Tendon healing involves both endogenous and exogenous healing processes. Endogenous healing occurs within the tendon itself, primarily relying on the proliferation and differentiation of the tendon's cells, such as fibroblasts, tenocytes, and inflammatory cells, to produce new, well-organized collagen fibers. This endogenous healing results in a repair that closely resembles the original tendon tissue.[35] Exogenous healing, on the other hand, is the main cause of tendon adhesions. It depends on the migration of cells from the surrounding tissues, such as skin, muscle, and adipose tissue, to the injury site, where they produce irregular collagen fibers, ultimately leading to scar formation.

In this experiment, we synthesized a novel material, RCDs/UA@Lipo-HAMA, and applied it locally around the sutured tendon tissue. RCDs/UA@Lipo-HAMA act on the tendon periphery (exogenous healing process), inhibiting scar tissue formation and preventing adhesions between the tendon and surrounding tissues. Additionally, RCDs/UA@Lipo-HAMA slowly release RCDs and UA, which strongly inhibit oxidative stress, inflammation, and fibrosis during the exogenous healing process, effectively preventing the formation of adhesions in the surrounding tissues. Using a modified Kessler method to tightly suture the damaged tendon results in poor drug penetration. Therefore, RCDs/UA@Lipo-HAMA minimally interfere with the endogenous healing process, facilitating normal internal repair of the tendon. Thus, RCDs/UA@Lipo-HAMA prevents tendon adhesions without significantly affecting tendon healing. In animal experiments, we found that RCDs/UA@Lipo-HAMA improved collagen arrangement and biomechanical properties, reduced tendon adhesion, and promoted motor function after tendon injury. It not only facilitated tendon healing but also effectively reduced adhesions between the injured tendon and surrounding tissues.

Tendon adhesion is essentially a fibrotic disease caused by excessive deposition of ECM in the peritendinous tissues, leading to fibrosis and restricted tendon gliding.[35] The inflammatory and proliferative phases are crucial stages in tendon healing. During these phases, the injured tendon triggers inflammation, resulting in increased cell damage and metabolism and producing a large amount of free radicals.[13] At this time, the balance between oxidative and antioxidative systems in the tendon is disrupted, leading to an excess of ROS and causing oxidative stress.[14] Oxidative stress recruits and stimulates more leukocytes, exacerbating the inflammatory response in the tendon, and leading to increased tendon proliferation and fibrosis.[3,36] Studies have shown that the NRF2/HO-1 signaling pathway is a crucial mechanism for cells to respond to oxidative stress.[37] Under oxidative stress conditions, NRF2 separates from Keap1 and translocates into the nucleus. In the nucleus, NRF2 binds to antioxidant response elements (ARE) and initiates the expression of antioxidant genes such as HO-1.[38,39] HO-1 breaks down heme to produce antioxidant and anti-inflammatory byproducts, protecting cells from oxidative damage and reducing inflammation. In this experiment, RCDs/UA@Lipo increased the total amount of NRF2 and promoted its nuclear translocation, resulting in increased expression of antioxidant proteins like HO-1, thereby enhancing the cells' antioxidant capacity. Studies have found that RCDs can scavenge various free radicals, reduce ROS levels, and inhibit the release of inflammation-related factors such as TNF-α, IL-6, and IL-1β.[21] Fu et al discovered that ursolic acid reduces oxidative stress damage in myocarditis by activating the Nrf2/HO-1 signaling pathway.[40] In this experiment, RCDs/UA@Lipo-HAMA slowly releases RCDs and UA, activating the Nrf2/HO-1 signaling pathway. As a result, RCDs/UA@Lipo-HAMA effectively reduces tendon fibrosis and adhesions. Adhesion scores, biomechanical, gait assessments, and tendon gliding experiments showed that the tendon quality after RCDs/UA@Lipo-HAMA treatment was significantly better than that of the single-drug groups (RCDs@Lipo-HAMA and UA@Lipo-HAMA), highlighting the effectiveness of the dual-drug loading strategy.

For the first time, we synthesized a novel material, RCDs/UA@Lipo-HAMA, to prevent tendon adhesion. The considerations for designing this system were as follows: 1) RCDs possessed SOD-like enzyme activity,[41,42] and UA possesses both antioxidant and anti-inflammatory properties.[43,44] Together, they synergistically enhance the inhibition of oxidative stress and inflammation at the initial stage of tendon injury; 2) RCDs were dispersed in water, while UA had poor aqueous solubility; thus, they were rationally co-encapsulated into the hydrophilic cavity and hydrophobic phospholipid bilayer interlayer of liposomes, respectively; 3) Liposomes can promote the uptake of RCDs and UA by cells and tissues through membrane fusion,[45] and then achieve rapid clearance of ROS by RCDs to inhibit the progression of antioxidant, along with the continuous anti-oxidative and anti-inflammatory effects of UA, and ultimately

RCDs/UA@Lipo achieved anti-fibrotic effects; and 4) The incorporation of the HAMA hydrogel allows for the swift solidification of the composite under UV light irradiation. This feature ensures the immobilization and sustained release of RCDs/UA@Lipo at the site of tendon injury, promoting effective and localized therapeutic action. The main limitation of this experiment is the small sample size, which may reduce statistical significance and representativeness; future research should increase the sample size to enhance credibility and generalizability.

The intraoperative application of RCDs/UA@Lipo-HAMA serves dual functions: it minimizes the leakage of nanomedicines through its light-curing properties and acts as a physical barrier, effectively mitigating tendon adhesion and fibrous tissue proliferation. The composite's superior biocompatibility and biodegradability ensure its safe, long-term use without eliciting rejection or inflammatory responses. Importantly, it does not obstruct nutrient diffusion, a critical factor for wound healing and tendon mobility. In summary, RCDs/UA@Lipo-HAMA delivers potent antioxidant and anti-inflammatory benefits, curtails fibroblast transdifferentiation, minimizes tissue fibrosis, and alleviates tendon adhesion.

Conclusion

In this study, we developed a novel composite biomaterial, RCDs/UA@Lipo-HAMA, aimed at preventing adhesion following tendon injuries. Stable and sustained release of the RCDs and UA at the injured tendon sites was achieved. The application of RCDs/UA@Lipo-HMA could attenuate oxidative stress by facilitating the upregulation of the Nrf2/HO-1 pathway. It effectively prevented macrophage aggregation and inhibited TGF-β1-induced fibroblast transdifferentiation, thereby reducing inflammation and fibrosis. Consequently, RCDs/UA@Lipo-HAMA significantly reduced tendon adhesion formation and promoted tendon healing. This study provided a novel therapeutic approach for the clinical treatment of tendon injuries.

Acknowledgments

We wish to express our profound gratitude to Dr. Huanfa Yi for his important comments and valuable suggestions on this manuscript, and the support of the central laboratory. This study was financially supported by the National Natural Science Foundation of China (NSFC, under Grant Nos. 82101454), the JLU Science and Technology Innovative Research Team (2017TD-06).

Disclosure

The authors report no conflicts of interest in this work.

References

1. Asplund CA, Best TM. Achilles tendon disorders. *BMJ*. 2013;346(mar12 1):f1262–f1262. doi:10.1136/bmj.f1262
2. Schneider M, Angele P, Järvinen TAH, Docheva D. Rescue plan for Achilles: therapeutics steering the fate and functions of stem cells in tendon wound healing. *Adv Drug Delivery Rev*. 2018;129:352–375. doi:10.1016/j.addr.2017.12.016
3. Nourissat G, Berenbaum F, Duprez D. Tendon injury: from biology to tendon repair. *Nat Rev Rheumatol*. 2015;11:223–233. doi:10.1038/nrrheum.2015.26
4. Millar NL, Murrell GAC, McInnes IB. Inflammatory mechanisms in tendinopathy – towards translation. *Nat Rev Rheumatol*. 2017;13:110–122. doi:10.1038/nrrheum.2016.213
5. Vinhas A, Almeida AF, Rodrigues MT, Gomes ME. Prospects of magnetically based approaches addressing inflammation in tendon tissues. *Adv Drug Delivery Rev*. 2023;196. doi:10.1016/j.addr.2023.114815
6. Magnusson SP, Langberg H, Kjaer M. The pathogenesis of tendinopathy: balancing the response to loading. *Nat Rev Rheumatol*. 2010;6:262–268. doi:10.1038/nrrheum.2010.43
7. He P, Ruan D, Huang Z, et al. Comparison of Tendon Development Versus Tendon Healing and Regeneration. *Front Cell Develop Biol*. 2022:10. doi:10.3389/fcell.2022.821667
8. Cartucho A. Tendon transfers for massive rotator cuff tears. *EFORT Open Reviews*. 2022;7:404–413. doi:10.1530/eor-22-0023
9. Tan V, Nourbakhsh A, Capo J, et al. Effects of nonsteroidal anti-inflammatory drugs on flexor tendon adhesion. *J Hand Surg Am*. 2010;35:941–947. doi:10.1016/j.jhsa.2010.02.033
10. Jiang S, Zhao X, Chen S, et al. Down-regulating ERK1/2 and SMAD2/3 phosphorylation by physical barrier of celecoxib-loaded electrospun fibrous membranes prevents tendon adhesions. *Biomaterials*. 2014;35:9920–9929. doi:10.1016/j.biomaterials.2014.08.028
11. Chen S, Jiang S, Zheng W, et al. RelA/p65 inhibition prevents tendon adhesion by modulating inflammation, cell proliferation, and apoptosis. *Cell Death Dis*. 2017;8:e2710. doi:10.1038/cddis.2017.135
12. Lui PPY, Zhang X, Yao S, Sun H, Huang C. Roles of Oxidative Stress in Acute Tendon Injury and Degenerative Tendinopathy—A Target for Intervention. *Int J Mol Sci*. 2022;23. doi:10.3390/ijms23073571
13. Morry J, Ngamcherdtrakul W, Yantasee W. Oxidative stress in cancer and fibrosis: opportunity for therapeutic intervention with antioxidant compounds, enzymes, and nanoparticles. *Redox Biol*. 2017;11:240–253. doi:10.1016/j.redox.2016.12.011

14. Piera-Velazquez S, Jimenez SA. Oxidative Stress Induced by Reactive Oxygen Species (ROS) and NADPH Oxidase 4 (NOX4) in the Pathogenesis of the Fibrotic Process in Systemic Sclerosis: a Promising Therapeutic Target. *J Clin Med*. 2021;10. doi:10.3390/jcm10204791
15. Hu -H-H, Chen D-Q, Wang Y-N, et al. New insights into TGF-β/Smad signaling in tissue fibrosis. *Chem Biol Interact*. 2018;292:76–83. doi:10.1016/j.cbi.2018.07.008
16. Yang Z, Xu T, Li H, et al. Zero-Dimensional Carbon Nanomaterials for Fluorescent Sensing and Imaging. *Chem Rev*. 2023;123:11047–11136. doi:10.1021/acs.chemrev.3c00186
17. Liu J, Li R, Yang B. Carbon Dots: a New Type of Carbon-Based Nanomaterial with Wide Applications. *ACS Cent Sci*. 2020;6:2179–2195. doi:10.1021/acscentsci.0c01306
18. Wang B, Cai H, Waterhouse GIN, et al. Carbon Dots in Bioimaging, Biosensing and Therapeutics: a Comprehensive Review. *Small Science*. 2022:2. doi:10.1002/smsc.202200012
19. Yang M, Li H, Liu X, et al. Fe-doped carbon dots: a novel biocompatible nanoplatform for multi-level cancer therapy. *J Nanobiotechnol*. 2023:21. doi:10.1186/s12951-023-02194-6
20. Yang M, Su B, Ma Z, et al. Renal-friendly Li(+)-doped carbonized polymer dots activate Schwann cell autophagy for promoting peripheral nerve regeneration. *Acta Biomater*. 2023;159:353–366. doi:10.1016/j.actbio.2023.01.027
21. Liu C, Fan W, Cheng WX, et al. Red Emissive Carbon Dot Superoxide Dismutase Nanozyme for Bioimaging and Ameliorating Acute Lung Injury. *Adv Funct Mater*. 2023:33. doi:10.1002/adfm.202213856
22. Wu S, Shi Y, Jiang L, et al. N-Acetylcysteine-Derived Carbon Dots for Free Radical Scavenging in Intervertebral Disc Degeneration. *Adv. Healthcare Mater*. 2023:12. doi:10.1002/adhm.202300533
23. Zhang J, Yang M, Tang X, et al. Intestinal delivery of ROS-scavenging carbonized polymer dots for full-course treatment of acute and chronic radiation enteritis. *Appl Mater Today*. 2022:28. doi:10.1016/j.apmt.2022.101544
24. Wang X, Ikejima K, Kon K, et al. Ursolic acid ameliorates hepatic fibrosis in the rat by specific induction of apoptosis in hepatic stellate cells. *J Hepatol*. 2011;55:379–387. doi:10.1016/j.jhep.2010.10.040
25. Wang X-T, Gong Y, Zhou B, et al. Ursolic acid ameliorates oxidative stress, inflammation and fibrosis in diabetic cardiomyopathy rats. *Biomed Pharmacother*. 2018;97:1461–1467. doi:10.1016/j.biopha.2017.11.032
26. Dhakal H, Kim M-J, Lee S, et al. Ursolic acid inhibits FcεRI-mediated mast cell activation and allergic inflammation. *Int Immunopharmacol*. 2021:99. doi:10.1016/j.intimp.2021.107994
27. Liu X, Wei Y, Xuan C, et al. A Biomimetic Biphasic Osteochondral Scaffold with Layer-Specific Release of Stem Cell Differentiation Inducers for the Reconstruction of Osteochondral Defects. *Adv. Healthcare Mater*. 2020:9. doi:10.1002/adhm.202000076
28. Tang J, Ishii S, Masamichi U, Aoki M. Dorsal and Circumferential Sheath Reconstructions for Flexor Sheath Defect with Concomitant Bony Injury. *J Hand Surg*. 1994;19:61–69. doi:10.1016/0363-5023(94)90225-9
29. Wang S, Yao Z, Zhang X, et al. Energy-Supporting Enzyme-Mimic Nanoscaffold Facilitates Tendon Regeneration Based on a Mitochondrial Protection and Microenvironment Remodeling Strategy. *Adv Sci*. 2022:9. doi:10.1002/advs.202202542
30. Sun J, Ju F, Jin J, et al. M2 Macrophage Membrane-Mediated Biomimetic-Nanoparticle Carrying COX-siRNA Targeted Delivery for Prevention of Tendon Adhesions by Inhibiting Inflammation. *Small*. 2023:19. doi:10.1002/smll.202300326
31. Yuan Y, Zhai Y, Chen J, Xu X, Wang H. Kaempferol Ameliorates Oxygen-Glucose Deprivation/Reoxygenation-Induced Neuronal Ferroptosis by Activating Nrf2/SLC7A11/GPX4 Axis. *Biomolecules*. 2021;11. doi:10.3390/biom11070923
32. Sun -Y-Y, Zhu H-J, Zhao R-Y, et al. Remote ischemic conditioning attenuates oxidative stress and inflammation via the Nrf2/HO-1 pathway in MCAO mice. *Redox Biol*. 2023:66. doi:10.1016/j.redox.2023.102852
33. Zhou Z, Li S, Gong X. Polydopamine Nanoparticles-Based Photothermal Effect Against Adhesion Formation in a Rat Model of Achilles Tendon Laceration Repair. *Int j Nanomed*. 2023;18:1765–1776. doi:10.2147/ijn.S393454
34. Li S, Gong F, Zhou Z, Gong X. Combined Verapamil-Polydopamine Nanoformulation Inhibits Adhesion Formation in Achilles Tendon Injury Using Rat Model. *Int j Nanomed*. 2023;18:115–126. doi:10.2147/ijn.S377600
35. Wynn TA, Ramalingam TR. Mechanisms of fibrosis: therapeutic translation for fibrotic disease. *Nat Med*. 2012;18:1028–1040. doi:10.1038/nm.2807
36. Voleti PB, Buckley MR, Soslowsky LJ. Tendon Healing: repair and Regeneration. *Annual Rev Biomedical Engin*. 2012;14:47–71. doi:10.1146/annurev-bioeng-071811-150122
37. Zhang X, Yu Y, Lei H, et al. The Nrf-2/HO-1 Signaling Axis: a Ray of Hope in Cardiovascular Diseases. *Cardiol Res Pract*. 2020;2020:5695723. doi:10.1155/2020/5695723
38. Gong W, Li J, Chen Z, et al. Polydatin promotes Nrf2-ARE anti-oxidative pathway through activating CKIP-1 to resist HG-induced up-regulation of FN and ICAM-1 in GMCs and diabetic mice kidneys. *Free Radic Biol Med*. 2017;106:393–405. doi:10.1016/j.freeradbiomed.2017.03.003
39. Huang K, Chen C, Hao J, et al. Polydatin promotes Nrf2-ARE anti-oxidative pathway through activating Sirt1 to resist AGEs-induced upregulation of fibronetin and transforming growth factor-beta1 in rat glomerular messangial cells. *Mol Cell Endocrinol*. 2015;399:178–189. doi:10.1016/j.mce.2014.08.014
40. Fu Y, Liu T, He S, et al. Ursolic acid reduces oxidative stress injury to ameliorate experimental autoimmune myocarditis by activating Nrf2/HO-1 signaling pathway. *Front Pharmacol*. 2023;14:1189372. doi:10.3389/fphar.2023.1189372
41. Dehvari K, Chiu S-H, Lin J-S, et al. Heteroatom doped carbon dots with nanoenzyme like properties as theranostic platforms for free radical scavenging, imaging, and chemotherapy. *Acta Biomater*. 2020;114:343–357. doi:10.1016/j.actbio.2020.07.022
42. Wang H, Zhang M, Ma Y, et al. Carbon Dots Derived from Citric Acid and Glutathione as a Highly Efficient Intracellular Reactive Oxygen Species Scavenger for Alleviating the Lipopolysaccharide-Induced Inflammation in Macrophages. *ACS Appl Mate Interf*. 2020;12:41088–41095. doi:10.1021/acsami.0c11735
43. Wan SZ, Luo FY, Huang CK, et al. Ursolic acid reverses liver fibrosis by inhibiting interactive NOX4/ROS and RhoA/ROCK1 signalling pathways. *Aging-Us*. 2020;12:10614–10632. doi:10.18632/aging.103282
44. Gan D, Zhang W, Huang C, et al. Ursolic acid ameliorates CCl4-induced liver fibrosis through the NOXs/ROS pathway. *J Cell Physiol*. 2018;233:6799–6813. doi:10.1002/jcp.26541
45. Gandek TB, van der Koog L, Nagelkerke A. A Comparison of Cellular Uptake Mechanisms, Delivery Efficacy, and Intracellular Fate between Liposomes and Extracellular Vesicles. *Adv Healthcare Mater*. 2023;12. doi:10.1002/adhm.202300319